

Size, shape, composition, and electronic properties of InAs/GaAs quantum dots by scanning tunneling microscopy and spectroscopy

S. Gaan, Guowei He, and R. M. Feenstra

Dept. Physics, Carnegie Mellon University, Pittsburgh, PA 15213

J. Walker and E. Towe

Dept. Electrical and Computer Engineering, Carnegie Mellon University, Pittsburgh, PA 15213

Abstract

InAs/GaAs quantum dot heterostructures grown by molecular-beam epitaxy are studied using cross-sectional scanning tunneling microscopy and spectroscopy. The images reveal individual InAs quantum dots (QDs) having a lens shape with maximum base diameter of 10.5 nm and height of 2.9 nm. Analysis of strain relaxation of the QDs reveals an indium composition varying from 65% at the base of the QD, to 95% at its center, and back to 65% at its apex. Room-temperature tunneling spectra acquired 3-4 nm from the center of a dot show a peak located in the upper part of the GaAs bandgap originating from the lowest electron confined state of the QD, along with a tail in the conductance extending out from the valence band and originating from QD hole states. A computational method is developed for simulating the tunneling spectra using effective-mass bands treated in an envelope-function approximation. By comparison of the computations to low-current spectra, the energy of the lowest electron and highest hole QD states are determined. These energies are found to be in reasonably good agreement both with optical measurements and prior theoretical predictions of Wang *et al.* [Phys. Rev. B **59**, 5678 (1999)].

I. Introduction

Semiconductor quantum-dots (QDs) have been investigated extensively over the past decades,¹ with InAs QDs grown on GaAs being one of the most commonly studied materials system. These self-assembled dots can be grown using molecular beam epitaxy (MBE) in the Stranski-Krastanow growth mode. Common experimental methods for studying QDs generally yield information on only structural characteristics (size, shape, and composition), *e.g.* using electron microscopy or x-ray diffraction, or on spectroscopic properties (energies of confined states), *e.g.* using low-temperature photoluminescence. However, the combination of scanning tunneling microscopy and spectroscopy (STM/S) can in principle yield information on *both* types of properties. Such measurements have the benefit of eliminating the inhomogeneous broadening that is inherent in measurements that average over the distribution of quantum dots in a sample. Nevertheless, prior STM/S studies have focused primarily on the structural^{2,3,4,5,6} or the spectroscopic characteristics,^{7,8,9,10,11,12,13} with a complete determination of QD size, shape, composition, *and* electronic properties based solely on STM/S having not been reported to date. This type of experimental determination is the goal of the present work.

To accurately model experimental data relating to QDs it is important to develop a quantitative relationship between the QD size and the energy of its states. Two widely cited papers in the literature have developed theories of this sort, one based on nonlocal, empirical pseudopotentials¹⁴ and the other on an eight-band $\mathbf{k} \cdot \mathbf{p}$ method.¹⁵ Results for the two techniques generally agree in terms of the ordering and nature of the states, but the actual energies of the states for specific QD sizes differ significantly – for example, the energies of the lowest electron bound state differ by nearly a factor of 2 (subsequent work demonstrated that this discrepancy arose both from the parameters used in the computations as well as from the theoretical techniques *per se*).¹⁶ Comparison with experimental data for QDs of known size and shape is desirable in order to provide some measure of validation for the theories.

A prior study attempted such a comparison for lens-shaped QDs with base diameter of 25 nm and height 3.5 nm, but lack of experimental knowledge on the composition of the QDs inhibited a parameter-free comparison.¹⁷ A very recent study accomplished this type of comparison for InAs QDs with 24 nm base diameter and 7 nm height, by combining experimental results from STM and from optical spectroscopy, and this work then employed theoretical predictions to fine-tune the QD structural parameters.¹⁸ In contrast, in the present work we use STM/S measurements *alone* to extract both the structural and spectroscopic properties of QDs (albeit without the fine structural details as in Ref. [18]), and we then employ these results as a test for the validity of the prior theoretical predictions for the binding energies of the QD states.

In this work we study InAs quantum dots in GaAs, grown by MBE. From an analysis of cross-sectional STM images¹⁹ we find that the QDs have a lens-type shape, *i.e.* a section of a sphere, with maximum base diameter of 10.5 nm and height of 2.9 nm. The composition of the QDs is determined from an analysis of strain relaxation, examining both the displacement of the cleavage surface and the local lattice parameter, which yields a linearly varying indium content of 65% at the QD base, to 95% at its center, and back to 65% at its apex. In room-temperature tunneling spectroscopy, the lowest electron confined state of the QDs is clearly visible and a tail of states arising from the hole confined states also appears. A quantitative determination of the energy of these states is complicated by the fact that the observed spectral features are somewhat broad (due to both temperature and the effects of the modulation voltage used in the measurement) and they are also shifted along the voltage scale because of tip-induced band bending. Charging effects in the spectra are also apparent, as discussed in our prior publication.²⁰ We deal with these effects by employing low-current spectra, and modeling them with a theory that includes 3D electrostatic simulation of the tip-vacuum-semiconductor geometry²¹ together with computation of tunnel currents using a plane-wave solution of Schrödinger's equation in a supercell geometry. With this method, we are able to extract the energies of the lowest electron and highest hole confined states.

This paper is organized as follows. In the next section we present experimental results for both QD structure and spectroscopy. In section III we formulate our computational method for describing the tunnel current. In section IV we compare the computational results to experiment for the InAs/GaAs QDs, thereby permitting the evaluation of the

binding state energies of the deepest QD states. In Section V those energies are compared with both photoluminescence data from our samples and previous theoretical predictions for QDs of various sizes.^{14,15} Finally, the paper is summarized in section VI.

II. Experimental Results

A. Structure and Composition

The InAs/GaAs QD structures were grown using solid source MBE.²² On an n-type (001) oriented GaAs substrate, 200 nm of GaAs buffer layer was grown followed by 5 periods of InAs QDs. The QD layers were separated by 50 nm of GaAs. The superlattice was then capped with about 200 nm of GaAs overlayer. The GaAs buffer, spacer, and cap layers as well as the QDs were all nominally undoped. The GaAs was deposited at about 1 ML/s (ML = monolayer = 0.28 nm GaAs thickness), with the wafer held at 580°C. The InAs for the QD layers was deposited at 0.27 ML/s (ML = 0.30 nm InAs unstrained thickness) with the sample at 490°C, and using a deposition time of 10 s. This relatively large growth rate for the QDs is found to produce a high density of relatively small QDs, which lead to improved behavior of infra-red focal plane arrays made with similarly grown QDs.²³

Cross-sectional STM (XSTM) measurements were performed at room temperature in an ultra high vacuum chamber with base pressure $<5 \times 10^{-11}$ Torr. Samples were cleaved *in-situ* to expose atomically flat (110) surfaces for subsequent STM and scanning tunneling spectroscopy (STS) measurements. Commercial Pt-Ir tips were cleaned *in-situ* by electron bombardment prior to use. Images are acquired with a constant current of 0.1 nA, and at sample-tip voltages specified below. Conductance spectra are measured and normalized in the same manner as previously described, using a lock-in amplifier and modulation voltage of 50 mV.²¹ Normalization of constant-separation is accomplished using a factor of $\exp(2\bar{\kappa}\Delta s)$ where the voltage-averaged $\bar{\kappa}$ value is determined from experiment to be 7.5 nm^{-1} .

Figure 1 shows two representative STM images of our QDs. The QDs appear bright in the images because, after cleavage, they relax outwards due to the strain arising from the 7% lattice mismatch between InAs and GaAs. High-pass filtering of such images yields a more direct view of the cross-sectional QD shape,²⁰ as shown in Fig. 1 of our prior publication.²⁰ We find a cross-sectional shape consistent with either a truncated pyramid, a truncated cone, or a lens (section of a sphere), similar to that found by prior workers.^{4,6} Further definition of the QD shape can be obtained using the methodology of Bruls *et al.*⁴ in which the measured cross-sectional heights are plotted as a function of the measured cross-sectional base length, as shown in Fig. 2. The maximum base length along the $[1\bar{1}0]$ direction and height along the $[001]$ direction are seen to be $b=10.5 \pm 0.5$ and $h=2.9 \pm 0.2$ nm, respectively (this height *includes* the wetting layer). The distribution is seen to be consistent with 3-dimensional dot shapes of either a truncated cone or a lens, and we use the latter for further analysis. For this lens shape, the radius of the corresponding sphere is $R = [(b/2)^2 + h^2]/(2h) = 6.20 \text{ nm}$, and the maximum angle of

the sidewall to the base is 57.8° . The occurrence of this type of shape, for small QDs such as ours, is well explained in a recent work of Eisele *et al.*⁶

Topographic cuts through the QDs from Fig. 1(a) and 1(b) are shown in Fig. 3(a). These two QDs have cross-sections that are among the largest of any that we have studied, so that we can be confident that the cleavage plane has passed nearly through the center of the QDs. Assuming that electronic contributions to the images are small,²⁴ this cut can be compared to the results of finite-element analysis (continuum mechanics, including anisotropic effects²⁵) for a strained QD that is elastically relaxed at the cleavage surface. We consider our lens geometry with variable In composition x of the $\text{In}_x\text{Ga}_{1-x}\text{As}$ QD. At the same time, we match to data for the distance between corrugation maxima (local lattice parameter), shown in Fig. 3(b), measured along the same cut through the QDs as for the surface displacement of Fig. 3(a). We match the experimental data with finite-element computations made using a lens shape in the *unstrained* geometry with dimensions of $b=9.5$ and $h=2.6$ nm which correspond to, after strain, a distorted lens shape with $b=9.8$ and $h=2.9$ nm. We find agreement between experiment and theory for a linearly-graded In composition pictured in Fig. 3(a), varying from $x = 0.65$ at the bottom of the QD to $x = 0.95$ in the middle and back to $x = 0.65$ at the top of the QD.

The simultaneous fitting of the data in Figs. 3(a) and 3(b) provide strong constraints on the In composition. The average x -value (averaged over the [001] direction) of 0.80 is determined to an accuracy of a few %, and the grading of the x -value of 0.21 nm^{-1} is determined with an accuracy of around 20-30%. Prior works have indicated a grading profile that is much less steep in the lower part of the QD than the upper part.^{4,11,18} Our results are not inconsistent with that (*i.e.* at the limit of three times our estimated error range), although they favor the symmetric grading just mentioned. Separately, we note that for both data sets in Fig. 3(a) the experimental data are slightly higher than the finite-element results for spatial locations ≈ 1 nm above the apex of the QDs. We speculate that this discrepancy could arise from the presence of some excess In located in the GaAs *above* the QD, although we have not further investigated this possibility.

B. Electronic Spectroscopy

Spectra were acquired at various distances from the QDs; typical data for two dots are shown in Fig. 4. Let us first examine spectra A and M, acquired sufficient far (6 nm) from the center of the dots so that the results are typical of the pure GaAs(110) surface. A bandgap region is apparent in each spectrum, extending from about -0.5 to $+1.0$ V. Examining the spectra as the dot is approached, we observed in spectra C-D and P the appearance of the discrete state located ~ 0.2 eV below the GaAs conduction band (CB) edge. This peak is relatively sharp and well-defined, and we associate it with the lowest electron confined state of the QDs. A similar peak appears on the other side of the QDs, spectra K and W (the peak is somewhat broad in the former). However, at spatial locations closer to the QDs, it is seen in Fig. 4 that this peak broadens very substantially. As discussed in our prior work, we attribute this dramatic change in the spectra to the large currents passing through the dots which produce significant occupation of the (normally empty) electron confined states.²⁰

Similar type charging effects have been seen on other surfaces for which the transport of STM-injected current through the semiconductor is limited, such as neighboring dangling bonds on SiC(0001) $\sqrt{3}\times\sqrt{3}$ or isolated dangling bonds on boron-doped Si(111) $\sqrt{3}\times\sqrt{3}$.^{26,27} In the present case, the substantial separation between the neighboring QDs produces this limitation in the transport of the electrons. (It should be noted that our QDs and surrounding GaAs are *undoped*, in contrast to the substantial doping employed by some other workers in which case transport of the carriers from a QD to the surrounding semiconductor can readily occur^{9,13}). However, the current flowing through the QD when the tip is positioned 4 nm away from the dot center is about 50 times less than when the tip is right above the dot center (1.2 pA vs. 70 pA), and in the former case the current transport is apparently efficient enough to prevent any significant charging (broadening). The peak within the bandgap region observed when the tip is 4 nm from the dot center (~ 2 nm from the dot edge) arises, of course, from a tail of the wavefunction of the relevant QD confined state. Such wavefunction tails have been observed previously by STM/STS for numerous systems, including quantum dots.^{9,13}

Two other features in the spectra of Fig. 4 are notable. First, an atomic step is seen located about 6 nm away from the centers of both of the QDs, as marked on the images (see Fig. 1 of our prior work for a larger-scale view of such a step²⁰). For spectra acquired near the step, L and X, a distribution of states extending throughout the band gap (about -0.1 to 1.1 V) is apparent, arising from the step. Since our samples are undoped, this step acts to "pin" the Fermi-level (0 V in the spectra) at a location ~ 0.1 eV above the valence band (VB) maximum. Second, for the spectra associated with the QD of Fig. 4(b), some state-density is apparent throughout the bandgap region even for spectra acquired far from the atomic step. For example, in spectrum P, at voltages between about 0 and 0.7 V (*below* where the QD state occurs) a distribution of states is apparent. In additional spectra (not shown) we find that this distribution of states increases in magnitude for spectra acquired near the location marked "defect" in the image. A small depression, probably a vacancy, is seen at this location, and we thus associate this distribution of states with the vacancy. Apparently the vacancy-derived states are resonant with the QD states, forming the combined set of states occurring in spectra P – U.

III. Computational Method

To quantify the energy of the observed QD states we compare the experimental data with computed spectra, adjusting the VB and CB band offsets (and hence the energies of the confined states) to match theory and experiment. For each sample-tip voltage in a spectrum the 3D electrostatic problem of a hyperbolic-shaped probe-tip in proximity to a semiconductor is solved using a finite-element approach.^{21,28,29} The QD is treated as having the same dielectric constant as the surrounding semiconductor, and they are both undoped, so the dot has no impact on the electrostatics.³⁰ Figure 5 shows an example of this finite-element solution for the potential energy, including a source of surface state-density arising from surface steps as described in the following Section. Given the potential, the Bardeen formalism is used to compute the tunneling current. The

approximation of Tersoff and Hamann is also employed,³¹ assuming a sharp probe-tip for which case the tunnel current turns out to be proportional to the local density-of-state of the sample evaluated at the apex of the probe-tip. The expression for the current is then

$$I = \frac{8\pi\hbar e}{m} R^2 k_F \sum_{\mu} [f(E_{\mu}) - f(E_{\mu} - eV)] |\Psi_{\mu}(0,0,s)|^2 \quad (1)$$

where R is the tip radius-of-curvature, k_F is its Fermi wavevector, E_{μ} is the energy of an eigenstate of the sample, $f(E_{\mu})$ is the Fermi-Dirac occupation factor for that state, $f(E_{\mu} + eV)$ is the occupation factor for the corresponding state in the tip, V is the voltage of the sample relative to the tip, and $\Psi_{\mu}(0,0,s)$ is the wavefunction of the sample state evaluated at the position of the tip apex: $x = 0$, $y = 0$, and $z = s$ where s is the tip-sample separation. The prefactor of this expression differs from what we used in a prior work,²¹ and the source of this difference is explained in Appendix A. In comparing the absolute magnitude of the theoretical current with experiment, it should be borne in mind that our computations neglect any effect of the image potential in the vacuum, thus producing currents that are about 3 orders-of-magnitude smaller than those in experiment.²⁹

To evaluate Eq. (1), we consider the potential only in a small region around the tunnel junction, and we repeat this region periodically. For a periodic cell width $2w$ in the lateral (x,y) directions, we use sine and cosine basis states with wavevectors k_x or k_y equal to $n\pi/w$ (integer $n > 0$ for sine states and ≥ 0 for cosine states). For the z -direction perpendicular to the surface, the semiconductor is modeled as a slab of thickness $2a$ separated by a vacuum region of thickness $2(L - a)$. We consider both even (cosine) and odd (sine) basis states relative to the center of the slab. These states are matched to decaying exponentials in the vacuum, which yields the appropriate values for k_z . An effective mass m^* is assumed in the semiconductor and the free-electron mass m is used in the vacuum, so that this matching must be performed separately for each value of the parallel wavevector. Appendix B provides details of this procedure.

The basis states are thus labeled by wavevector, $\mathbf{k} \equiv (k_x, k_y, k_z)$, and our solution of the Schrödinger equation proceeds in the usual manner by expanding the eigenstates as

$$\Psi_{\mu}(x, y, z) = \sum_{\mathbf{k}} b_{\mathbf{k},\mu} \Phi_{k_x}(x) \Phi_{k_y}(y) \Phi_{k_z}(z) \quad (2)$$

and solving the eigenvalue problem $\sum_{\mathbf{k}'} H_{\mathbf{k},\mathbf{k}'} b_{\mathbf{k}',\mu} = E_{\mu} b_{\mathbf{k},\mu}$ with

$$H_{\mathbf{k},\mathbf{k}'} = \left(\pm \frac{\hbar^2 k^2}{2m^*} + E_0 \right) \delta_{\mathbf{k},\mathbf{k}'} + \langle k_x k_y k_z | \Delta V(x, y, z) | k'_x k'_y k'_z \rangle \quad (3)$$

where E_0 is the energy of the band edge, the plus sign is for a CB, and the minus sign is for a VB. ΔV is the change in potential relative to a simple tunneling problem with free-electron gas having effective mass m^* and with a flat tunnel barrier. Thus, ΔV includes

the electrostatic potential energy from the probe tip, from any charged steps or defects on the surface, and from the confining potential of the QD itself.

The resulting eigenvalues E_μ and eigenvectors $b_{\mathbf{k},\mu}$ are used to evaluate the tunnel current, Eq. (1). In this evaluation we encounter the well known limitation of the finite-size basis set which lead to unphysical zeroes in the wavefunctions in the vacuum region.³² To solve this problem, we use an approximate method for evaluating the wavefunction in the vacuum, according to $\Psi_\mu(0,0,s) = \Psi_\mu(0,0,0) \exp(-\beta_\mu)$ with

$$\beta_\mu = \int_0^s \left[2m(U(0,0,z) - E_\mu) / \hbar^2 + \langle k_{||}^2 \rangle_\mu \right]^{1/2} dz \quad (4)$$

where $U(0,0,z)$ is the potential energy in the vacuum and $k_{||}$ is the parallel wavevector. $U(0,0,z)$ is given by $\chi + E_C + \phi(0,0,z)$ where χ is the electron affinity, E_C is the CB minimum and $\phi(0,0,z)$ is the electrostatic potential energy which, by definition, equals zero at a point deep inside the semiconducting sample. This form for β_μ is the usual Wentzel–Kramers–Brillouin expression, and for a plane wave incident on the barrier one would use the *known* value of parallel wavevector within the square-root. In our problem, with the full wavefunctions *not* being plane waves, we use the expectation value of the parallel wavevector,

$$\langle k_{||}^2 \rangle_\mu = \sum_{\mathbf{k}} b_{\mathbf{k},\mu}^2 (k_x^2 + k_y^2) \quad (5)$$

where k_x and k_y are the known values for each basis state. This method neglects the dispersion (*i.e.* change in shape) of the wavefunctions in the vacuum, which, for the present problem involving relatively small $k_{||}$ values, should be a good approximation. For s -values less than about 0.5 nm we find that our approximate method produces wavefunction values in good agreement with the exact results from Eq. (2), and using the approximate method we can evaluate the wavefunctions out to arbitrarily large s -values.

Our computations are performed using effective-mass bands with masses of 0.0635 for the CB, and 0.081, 0.643, and 0.172 for the VBs, corresponding to GaAs values (our theoretical method requires identical masses in the QD and the surrounding material), all in terms of the free electron mass.³³ A value of 0.341 eV is used for the spin-orbit splitting.³³ Parameters in the computations are the tip radius-of-curvature, tip-sample separation, and sample-tip contact potential (work-function difference). As described in the following Section, in order to match the computations to experiment we also find it necessary to introduce a charge density associated with the atomic steps on the surface.

Regarding precision, our computations are performed for $n_k = 8$ k -values in each of the x , y , and z direction for VB states, and $n_k = 10$ values in each direction for CB states. Convergence of the tunneling current is reasonably good (the difference in localized state energies between the results given in the following Section and those obtained using 10 k -values in the VB and 12 in the CB is less than 50 meV for the VB or 5 meV for the

CB), but importantly, this convergence is not particularly important since we fit the final results to experiment in order to deduce the energies of confined states. The need for a sufficient number of k -value is only to produce a nicely continuous spectrum with shape that can be compared to experiment. We employ different energy cutoffs for each band owing to their different effective masses, designed to achieve reasonable convergence of the results and to produce a supercell size that is suitably larger than the QD size (or at least its height). The cutoffs E_{\max} are 6.0, 1.8, and 4.0 eV for the light-hole, heavy-hole, and split-off VBs, and 7.5 eV for the CB. The maximum k -values are $k_{\max} = \sqrt{2m^* E_{\max}} / \hbar$, the minimum nonzero k -values k_{\min} are k_{\max} / n_k , and the unit cell (supercell) sizes are $2\pi / k_{\min}$ which yields 14.1, 9.1, 11.8, and 17.8 nm, respectively, with the same length used for all three dimensions. A 2 nm wide vacuum region is used between the slabs. The number of grid points within the slab in each of the x , y , and z directions is taken to be $4n_k$. For these values, computation of a spectrum over 15 voltage points requires about 10 hours using a 2.7-GHz processor. Accomplishing the entire set of curve fits described in this paper required about six months of time on a cluster of 20 such processors.

For a homogeneous GaAs(110) surface we find that the results using the above computational method are in good agreement with those obtained using our prior method of numerical integration of Schrödinger's equation along the central axis of the problem,²⁹ as shown in Fig. 6. We divide the results of Eq. (1) by πR^2 here, so that the prefactor does not depend on tip radius (the only dependence on tip radius in Fig. 6 arises from increased tip-induced band bending for larger R). Completely separate computer programs are used for the two types of computations, so that the agreement between them provides a good check on the validity of the programs. At large voltages some small discrepancies occurs between the two methods, arising from the limited number of k -values and limited energy cutoffs in the plane-wave method. The method of numerical integration of Schrödinger's equation works well for a homogeneous semiconductor (it was also extended to handle the case of a wide quantum well by explicit construction of a basis set that exactly solves that problem in the lateral direction²¹), and computationally it is much faster than the plane-wave method. However, that method is inapplicable to the nonseparable problem of a quantum dot, and this reason that we had to develop the present plane-wave expansion method.

Considering the z -dimension in particular, our supercell size does not nearly encompass the full range of the tip-induced band bending region (>100 nm). It is this very limited extent of a supercell that led us in our prior work to avoid use of a plane-wave expansion, utilizing instead the numerical integration of Schrödinger equation in the z -direction.²⁹ However, based on the good agreement we have found on the results from the two methods (Fig. 6), we conclude that the plane-wave expansion does indeed capture the essential portions of the wavefunctions that make significant contributions to the current.

IV. Comparison of Theory and Experiment

A. Bare GaAs Spectrum

To compare the experimental results with the computations, we first consider spectrum A of Fig. 4(a), acquired sufficiently far from the QD so that the dot makes a negligible contribution. By fitting this spectrum of bare GaAs we can determine parameter values for the tip-sample separation s , tip radius-of-curvature R , and sample-tip contact potential $\Delta\phi$. The opening angle of the tip shank can also be varied in the computations, but we keep that fixed at 60° for all of our results (in previous computations we have generally used a 90° angle,^{21,29} but the tip radii for the present problem are rather small and so we use 60° to help prevent unnaturally small radii values in the curve fitting). The data is replotted in Fig. 7 as conductance at constant tip-sample separation, a quantity that is better suited to quantitative comparison of theory with experiment.³⁴ As in our prior work, we use the logarithm of the conductance in fitting the theory to experiment.²¹

Examination of Fig. 7 reveals a band gap region between $+0.5$ and -1.0 V, *i.e.* corresponding to an apparent gap of 1.5 eV which is only slightly larger than the known gap of GaAs (1.42 eV). We thus find that tip-induced band bending has only a small effect on the spectrum, a somewhat surprising result considering that the GaAs regions surrounding the QD layer are undoped. This lack of band bending can only arise from the presence of some midgap states on the surface that act to "pin" the Fermi-level. Surface steps are invariably found on our cleavage surfaces, presumably forming due to the high strain regions at the QDs. Such steps are seen in both Figs. 4(a) and 4(b), and midgap states associated with the steps appear in spectra L and X, respectively. We thus identify these states associated with the surface steps as being responsible for the relatively small amount of tip-induced band bending. We find typically 1 or 2 steps near each layer of QDs.

The states associated with the steps of Fig. 4, spectra L or X, are seen to be distributed across the band gap region. We therefore assume a model with a *constant* step-density σ across the gap, and with a charge neutrality level E_N above which the states are negative when filled and below which they are positive when empty. (*i.e.* acceptor-like or donor-like, respectively). To model the arrangement of steps, we firstly place a step at 6 nm from the QD, corresponding to Fig. 4(a). We then also include a step near each layer of QDs, *i.e.* located every 50 nm from the first step.³⁵ The only steps that contribute to the model are the first one, 6 nm from the layer of QDs under investigation, and the one 50 nm away from the first on the other side of the probe tip (this second step plays a crucial role in constraining the potential and thus influencing the computed spectra). Regarding the state-density σ , we find that a value corresponding to one state (*i.e.* dangling bond) per unit cell along the step (0.40 nm) per eV, or $2.5 \text{ nm}^{-1} \text{ eV}^{-1}$, produces a good fit to this GaAs spectrum;³⁶ this value seems quite reasonable for an atomic step. From the fitting we obtain values for all the parameters, as listed in Fig. 7. In the following section we consider the features arising from the QDs that modify this GaAs spectrum.

B. Quantum Dot Spectra

Results for tunneling spectra near the QD of Fig. 4(a) are displayed in Fig. 8, again plotted as conductance at constant tip-sample separation. The experimental data is shown

in the top part of the figure and theoretical results are shown at the bottom. The same parameter values are used here as for the model of Fig. 7, but we add additional parameters for the VB and CB offsets. The theoretical results are computed for a lens-shaped QD with cleavage plane extending through the center of the dot, and using dimensions (corresponding to a *strained* QD) of 2.9 nm height and 10.5 nm base diameter. We use the same In composition as determined from Fig. 3. The band offsets are taken to be proportional to In composition x , $\Delta E_{i,x} = x \Delta E_i$ with $i = V$ or C , with all values quoted below for the band offsets corresponding to the value of ΔE_i (*i.e.* for 100% In composition).

In the theoretical spectra of Fig. 8 a large peak is seen near +0.9 V arising from the lowest electron confined state of the QD. This same peak is seen in the experiment, at distances of 3-4 nm from the dot, but for the spectra acquired closer to the dot the peak is greatly broadened. As already discussed in Section II and in our prior work we attribute this effect to charging of the dot.²⁰ The peak near +0.9 V in the theory does not shift nor broaden significantly as the QD is approached (except for a shift to lower voltages for the computed spectrum at 0 nm from the dot center, which is caused by a large negative differential resistance region near 1.1 V, further discussed below, that distorts the shape of the 0.9 V peak). This absence of a shift reveals that the band bending at the tip position, which is largely determined by the surface step located 6 nm on the other side of the QD, is not changing significantly as the tip position is varied from 4 nm to 0 nm away from the QD.

On the VB side of the spectrum some possible charging effects are also apparent. At 4 nm from the QD the theoretical spectrum shows a tail in the conductance extending out from the VB, in agreement with the experiment, and below we will show that this tail originates from light-hole QD states. However, at closer distances to the QD the theoretical spectra show a considerable increase in conductance around -0.2 V that is *not* found in the experiment. This computed conductance arises from heavy-hole states, and it is likely that occupation (charging) of these states prevents any significant current through them.

Figure 9 compares experimental and theoretical results for the spectra acquired 4 nm from the dot, *i.e.* low current results not significantly affected by charging. In Fig. 9(a) we show the same results as from Fig. 8 in which we utilize the two parameters for the VB and CB offsets. We adjust the parameter values in order to approximately match the theory with the experiment. We find reasonable agreement in magnitude for the conductance peak ~ 0.2 V below the CB edge, as well as for the tail extending out from the VB. The latter is much smaller in amplitude than the former because of the larger light-hole mass compared to the electron mass (so that the wavefunction has decayed more at this 4-nm distance from the QD) as well as due to the greater separation from the band edge of the electron state compared to the hole state. Nevertheless, one glaring discrepancy between the theory and the experiment is the deep minimum in the computed conductance at about +1.1 V. The reason for this minimum is that only a *single* QD electron state occurs in the theory, as seen in the distribution of states shown below the spectrum. That distribution shows the voltages at which specific states that we compute

are aligned with the Fermi level of the probe-tip. These voltages thus correspond to the "position" of the states, on the voltage axis. We see that there is a single bound state derived from the CB, and one bound state derived from the light-hole VB (there are also 6 bound states derived with the heavy-hole VB but these make a negligible contribution to the conductance at this distance of 4-nm distance from the QD, and similarly for the split-off VB). Also shown by the hatched regions are the continua of states associated with the unconfined VB and CB in the near-surface region.³⁷

As discussed in our prior work,²⁰ in order to achieve a better fit between experiment and theory it is necessary to include one additional parameter describing the QDs, namely, a scale factor α for their size. The reason for this is that with our effective-mass (envelope function) theory the *number* of states for a given quantum dot size is underestimated.¹⁶ That is, even if one adjust the band offsets in order to produce a deepest (lowest electron or highest hole) state that agrees with the experiment then, if we use the actual QD size in the computation, the next highest electron state (or next lowest hole state) will be significantly too high (or low) in the theory. However, by adjusting the size of the QD, and simultaneously varying the band offsets in order to keep the energy of the deepest states approximately constant, we can achieve a good fit to the spectra over the entire range of energies.

Figure 9(b) shows the result using three parameters, the two band offsets and α . A good fit to the experiment is obtained. In the theory, a second electron state associated with the QD occurs, located very close to the GaAs CB minimum, and this state serves to eliminate the conductance minimum found in Fig. 9(a). To further investigate this state near the CB minimum, we plot in Fig. 10 computed local densities-of-states (LDOSs) for the two models from Fig. 9 and also for a model in which no QD is present. These computations are performed neglecting any band bending from the probe tip or surface steps. The LDOS is formed in the usual way by summing over all the states, representing each by a Gaussian of FWHM 0.055 eV, and weighting each state by the magnitude of the wavefunction on the surface at the center of the QD. For the two curves in Fig. 10 with the QD present, the electron bound state is apparent near 0.2 eV below the CB edge. Additionally, we see near the CB minimum (0 eV on the plot) distinct differences between the curves. For the model in which no α parameter is used, the LDOS is much lower than without any QD. Thus, an *anti-resonance* occurs in this model, and this anti-resonance accounts for the very low conductance found in the computed spectrum of Fig. 9(a) near +1.1 V. In contrast, for the model including the α parameter, the LDOS is *higher* around the CB minimum than in the absence of the QD, indicating the presence of a bound state at that energy. Within the accuracy of our parameters we cannot distinguish whether this state is a resonance or is truly localized (*i.e.* whether its energy is slightly above or below the CB edge), but this difference is unimportant so far as the computed conductance is concerned. In both cases the effect of the second confined electron state is to fill in the computed conductance near +1.1 V, thus producing the good fit between theory and experiment seen in Fig. 9(b).

The values for the ΔE_V , ΔE_C , and α parameters listed in Fig. 9(b) were obtained by performing a least-square fit for *fixed* values of s , R , $\Delta\phi$, σ , and E_N , *i.e.*, using the

central values from Fig. 7. In order to obtain a full estimation of the error ranges it is necessary to vary all eight parameters and simultaneously fit both the GaAs spectrum of Fig. 7 and the QD spectrum of Fig. 9. We have performed this task, with the result shown in Fig. 3 of our prior work.²⁰ In addition to these eight nonlinear parameters we have one linear parameter which is the overall amplitude for both spectra. We employ constant-current conditions between the two spectra in the computation so that only a single amplitude parameter is needed rather than two of them. The linear parameter is optimized at each iteration, and we search for the optimal values of the other parameters. A simplex search is used to optimize values of s , R , and $\Delta\phi$, and an extensive series of grid searches is used for the other nonlinear parameters. In this manner we obtain slightly different values for the parameters than those listed in Fig. 9(b), and most importantly we obtain a complete estimate of their errors. In particular, we find the values $\Delta E_V = 0.30 \pm 0.03$ eV, $\Delta E_C = 0.64 \pm 0.02$ eV, and $\alpha = 1.50 \pm 0.02$.

As discussed in our prior work,²⁰ the values for the band offsets derived by our fitting procedure are somewhat model dependent. But if we focus on the actual *energy* of the confined states rather than the band offsets, the result of the analysis is then quite *independent* of details of the model, since we are directly deducing the energies from a fit to the data. We extract the energies of the confined states by performing an identical computation as above but *without* the presence of any band bending due to the probe tip or the surface steps. This procedure yields an energy for the lowest electron confined state of 0.196 ± 0.012 below the CB minimum, and an energy of the highest light-hole state of 0.052 ± 0.015 above the VB maximum. It is these two states that are directly seen in the experiment, the former by the large peak near +0.9 V in the spectra and the latter by the weak tail in conductance extending out from the VB, with their error ranges given by the fitting of the theory to experiment. Using the theory, we can also determine the energy of the highest heavy-hole state: 0.185 ± 0.023 above the VB maximum.

V. Discussion

Using our STS data together with the lineshape analysis, we are able to deduce the energies of the deepest electron and hole QD states. Additionally, we have some indication from the LDOS of Fig. 10 of a second QD electron state located very near the CB minimum. This second state is quite interesting, since it is the dominant "receiving" state for infra-red optical detectors,³⁸ and as mentioned in Section II the growth recipe used for our QDs has been found to produce optimal properties for such devices.²³ The results of Fig. 10 indicate that this receiving state does in fact exist as a localized state for our QDs. (We have also computed this LDOS for larger numbers of k-points, up to $n_k=16$, with correspondingly larger unit cells in the theory, and the resonant/anti-resonant behavior near 0 eV for the two fitting models is fully present in all cases).

In combined experimental and theoretical work, Urbietta *et al.* have recently demonstrated that the energy of the lowest (highest) electron (hole) confined state of an InAs/GaAs QD vary only slightly ($\lesssim 5$ meV for electrons or $\lesssim 15$ meV for holes) between an embedded dot and a cleaved dot.¹¹ Therefore, we can compare our observed energies

with those for embedded dots. Low-temperature (77 K) photoluminescence spectra from our samples reveals a peak emission wavelength of $1.12 \mu\text{m} = 1.11 \text{ eV}$, very similar to that obtained in our prior work.²² Correcting for temperature,²⁰ we estimate this energy difference to be 1.05 eV at room temperature, which agrees with the energy difference from our STS results of $1.42 - (0.196 \pm 0.012) - (0.185 \pm 0.023) = 1.039 \pm 0.026 \text{ eV}$.

Our STS result can also be compared with prior theoretical predictions for embedded dots, as shown in the work of Wang *et al.* and of Stier *et al.*^{14,15} These prior works deal with pyramidal QDs with 100% In anion content having (110) sidewalls and sitting on a uniform wetting layer. Using our experimentally determined parameters values for ΔE_V , ΔE_C , and α , we apply our computational method to that type of QD. We consider an *unstrained* base length of 11.3 nm , a case that has been analyzed in detail in Ref. [14] and for which the volume of the QD is not too much different than that of our observed lens-shaped QDs. We find binding energies for the deepest electron and hole states of 0.36 ± 0.02 and $0.26 \pm 0.03 \text{ eV}$, respectively. The error values here reflect the experimental uncertainty in our parameter determination, and additional errors of about $\pm 0.01 \text{ eV}$ should be added to those values due to our extrapolation from lens-shaped to pyramidal-shaped QDs. For this same size QD, the empirical pseudopotential theory of Wang *et al.* produces binding energies of 0.32 and 0.24 eV for the deepest electron and hole states, respectively, whereas the $\mathbf{k} \cdot \mathbf{p}$ results of Stier *et al.* yield energies of 0.20 and 0.15 eV , respectively (using their results obtained with the valence-force-field model for strain). Our results are slightly higher than the predictions of Wang *et al.*,¹⁴ but are very much higher than those of Stier *et al.*⁴ It thus appears that the former theory provides a much better quantitative description of the QDs than the latter.

Let us now consider the reproducibility of the spectral results as measured on different QDs and also using different probe tips. Figure 11 shows a summary of data for six QDs. In our experiments we tended to focus on the largest apparent QDs, thus corresponding to cleavage planes that pass nearly through, or above, the center of the QD (*i.e.* so that $\geq 50\%$ of the dot remains). The results of Figs. 11(a) and 11(b) are the same as for Figs. 4(a) and (b), but including a few more individual spectra averaged into the total conductance curves. Figure 11(c) shows a different QD, but measured during the same experiment and displaying results quite similar as for Figs. 11(a) and 11(b). The remaining spectra of Figs. 11(d) – 11(f) were all measured during separate experiments (using different probe tips). The spectra of Fig. 11(d) reveal an unusual VB feature near -1.2 V , possibly arising from some specific states on the probe tip (or perhaps associated with specific states of the surface steps), but nevertheless comparing the spectra acquired on and off the QD reveals a difference that is in reasonable agreement with Figs. 11(a), 11(b), and 11(c). The results of Fig. 11(e) are again similar, although it displays a somewhat larger shift in the apparent VB onset measured on the QD compared to off of it. The particular QD probed here is the same one as shown in Fig. 1(a).

Finally, for the QD of Fig. 11(f), the tip-induced band bending is somewhat larger (*i.e.* larger apparent band gap on the GaAs) compared to the other results, but again the spectra are similar to the others. This particular spectrum was acquired from the QD

pictured in Fig. 1(b). Overall, there does appear to be a ≈ 0.1 eV shift from QD to QD in the apparent position of their confined states, with this variation possibly being affected by tip to tip variability and/or variations in band bending (*e.g.* due to proximity of surface steps to the QDs). It should be noted, however, that a 0.1 eV variation is the same size as the inhomogeneous broadening known to exist from PL spectra for QDs grown with the same growth method.²² In any case, the results of Fig. 11(a), which we have analyzed in details in Figs. 7, 8 and 9, are seen to fall near the middle of the spread of results found for the other QDs.

VI. Summary

In summary, we have employed STM and STS to probe both the structure and the electronic states associated with InAs QDs in GaAs. Cross-sectional imaging permits a determination of the shape of the dots (lens shaped, with maximum size of 10.5 nm base length and 2.9 nm height). Observation of the displacement of the dot profile out from the cleavage surface, together with its local lattice parameter, leads to an accurate determination of the cation composition as varying from 65% indium at the base of the QD to 95% at its center and back to 65% at its apex. In spectroscopy the lowest electron confined state is clearly observed, and a tail of states extending out from the VB is also seen and associated with the highest lying light-hole state. However, charging of the dots is found to be a significant problem, producing large amounts of broadening of the spectroscopic signature of the electron confined state for high tunnel currents. From low current results, and using a newly developed plane wave expansion method for computing the tunnel current and fitting to experiment, energies of the lowest electron and highest (heavy) hole states are found to be 0.20 ± 0.01 eV below the CB minimum and 0.19 ± 0.02 eV above the VB maximum, respectively. These results are in good agreement with photoluminescence results from the same wafer. Comparing to prior theoretical predictions for the energies of the confined states, for pyramidal dots with comparable size and scaling the experimental results to 100% indium composition, we find that the experimental results are in reasonably good agreement with the theoretical predictions of Wang *et al.*¹⁴ but differ considerably from the predictions of Stier *et al.*,¹⁵ thus providing a measure of validity for the former theory.

Acknowledgements

This work was supported by the National Science Foundation, grant DMR-0856240. Computing resources were provided by the McWilliams Center for Cosmology at Carnegie Mellon University. Discussions with H. Eisele, R. Goldman, and B. Grandidier are gratefully acknowledged.

Appendix A

The approximation of Tersoff and Hamman for the tunneling matrix element of a sharp tip was utilized by them in Ref. [31] to obtain an expression for the tunneling current, assuming a small voltage between sample and tip. For our computations it is necessary to generalize this to the case of larger voltages. We have previously performed this generalization, in Ref. [21], but we employed a somewhat *ad hoc* argument in doing so. Here we describe a more rigorous derivation of the result. The probability of tunneling between states μ and ν of the sample and tip, respectively, is given by^{39,40}

$$P = \frac{2\pi}{\hbar} \sum_{\mu,\nu} M_{\mu\nu}^2 [f(E_\mu) - f(E_\nu)] \delta(E_\mu - E_\nu - eV) \quad (\text{A1})$$

where $M_{\mu\nu}$ is the matrix element for the process, V is the voltage on the sample relative to the tip, and $f(E) = [1 + \exp((E - E_F)/kT)]^{-1}$ is a Fermi-Dirac occupation factor for Fermi-energy E_F . We use the result of Tersoff and Hamann for the matrix element,

$$M_{\mu\nu} = \frac{4\pi\hbar^2}{2m} \frac{1}{\sqrt{\Omega}} R e^{-\kappa R} \Psi_\mu(\mathbf{r}_0) \quad (\text{A2})$$

where Ω is the tip volume, R is the tip radius-of-curvature, \mathbf{r}_0 is the point at the center of radius-of-curvature of the tip, and κ is the inverse decay length of the wavefunctions in the vacuum. We write this expression using the wavefunction at the tip apex rather than at \mathbf{r}_0 , $\Psi_\mu(0,0,s) = e^{-\kappa R} \Psi_\mu(\mathbf{r}_0)$ (for states with small $k_{||}$); we prefer to use $\Psi_\mu(0,0,s)$ rather than $\Psi_\mu(\mathbf{r}_0)$ in our evaluation since the former has greater physical significance in terms of the magnitude of the tunnel current.

The sum over tip states is evaluated by converting it to an integral over energy and using a usual density-of-states of a free-electron gas, $\Omega k_\nu m / 2\pi^2 \hbar^2$. The integral over energy is then evaluated with the use of the δ -function from Eq. (A1), leaving the factor of k_ν (evaluated at energy $E_\nu = E_\mu - eV$) which is taken to be the Fermi-wavevector for the tip, k_F , in the limit of large k_F . Evaluating the tunnel current as $2eP$ (the factor of 2 for spin), we arrive at the expression in Eq. (1) of the main body of the paper. The prefactor there results differs by a factor of $(\kappa/k_F)^2$ from that which we previously obtained in Ref. [21]. This factor is of order unity ($\kappa \approx 10 \text{ nm}^{-1}$ and $k_F \approx 15 \text{ nm}^{-1}$) and has relatively little energy dependence, so this difference is not so significant. Additionally, Tersoff argues that the prefactor actually depends on additional aspects of the probe-tip electronic structure.⁴¹ In any case, we feel that the present derivation is an improvement over that in Ref. [21], and hence we use it here for all our computational results. In comparing the absolute magnitude of the current from Eq. (1) with experiment, it is important to note that the tip radius R may differ from that used in the electrostatic

tip-induced band bending solution, since, for relatively blunt tips, the current will likely be emitted from some small protrusion at the end of the tip.

Appendix B

We derive here certain properties for a set of basis functions that vary as a sine or cosine function within a semiconductor slab and are matched to sinh or cosh functions in the vacuum region on either side of the slab. We start by considering the 3-dimensional planar tunneling problem for a conduction band having effective mass m^* and with the band edge located at an energy V_0 below the vacuum level. The electron mass in the vacuum is the free-electron mass, m . This problem can be reduced to a 1-dimensional one involving only the perpendicular components of the wavefunctions, but since the masses differ between semiconductor and vacuum it is necessary to use a modified form for the barrier, as given below.

Taking the semiconductor slab to extend from $-a$ to $+a$, and with periodic repetition of the entire problem at the boundaries $-L$ and $+L$, we find the solutions for even-parity perpendicular wavefunctions of confined slab states to be

$$\Phi_{k_z}(z) = \begin{cases} c_1 \cos(k_z z), & -a < z \leq a \\ c_2 \cosh[K(L-z)], & a < z \leq L \\ c_2 \cosh[K(z-L)], & -L < z \leq -a \end{cases} \quad (\text{B1})$$

with $\hbar^2 k_z^2 / (2m^*) = E_\perp$ and $\hbar^2 K^2 / (2m) = \tilde{V}_0 - E_\perp$, where $E_\perp < \tilde{V}_0$ is the perpendicular component of the energy (in the semiconductor) relative to the band edge. The modified barrier term \tilde{V}_0 is given by

$$\tilde{V}_0 = V_0 - \frac{\hbar^2 k_{||}^2}{2m} \left(\frac{m}{m^*} - 1 \right) \quad (\text{B2})$$

where $k_{||}$ is the parallel component of the wavevector. Solutions for k_z and K are obtained by applying the boundary conditions at the surfaces of the slab of continuity of the wavefunction and the wavefunction derivative divided by m^* . Following Ref. [42], we define $\xi \equiv k_z a$ and $\eta \equiv Ka$, leading to the implicit equations for ξ and η of

$$\xi \tan \xi = \frac{m^*}{m} \eta \tanh(\alpha \eta) \quad (\text{B3a})$$

and

$$\frac{\xi^2}{m^*} + \eta^2 = c^2 \quad (\text{B3b})$$

where $\alpha \equiv (L/a) - 1$ and $c = \sqrt{2m\tilde{V}_0} a / \hbar$. In a similar manner as for the graphical solution of Ref. [42] (which was made for the simpler case with $m = m^*$ and $L \rightarrow \infty$), we find one solution for each value of ξ over the ranges $(n-1)\pi/2$ to $n\pi/2$ with

$n=1,3,5,\dots$ up to a maximum ξ value of $c\sqrt{m^*}$. We find that a suitable iterative scheme to evaluate these solutions for ξ and η is to use for the $(i+1)^{\text{st}}$ iteration

$$\xi^{(i+1)} = \tan^{-1} \left(\frac{m^*}{m\xi^{(i)}} \eta^{(i)} \tanh(\alpha\eta^{(i)}) \right) + (n-1)\frac{\pi}{2} \quad (\text{B4})$$

where the branch of \tan^{-1} between $-\pi/2$ and $\pi/2$ is assumed, $\eta^{(i)} \equiv \sqrt{c^2 - (\xi^{(i)})^2 / m^*}$, and we take $\xi^{(0)} = n\pi/2$. This scheme is applicable up to a maximum odd n value such that $n\pi/2 \leq c\sqrt{m^*}$. If, for the next odd n value, $c\sqrt{m^*}$ has a value such that $(n-1)\pi/2 \leq c\sqrt{m^*} < n\pi/2$, then a final solution exists with $(n-1)\pi/2 \leq \xi \leq c\sqrt{m^*}$. In this case we employ a simple 1D numerical search to find that solution.

For odd parity confined states of the conduction band the perpendicular wavefunctions are

$$\Phi_{k_z}(z) = \begin{cases} c_1 \sin(k_z z), & -a < z \leq a \\ c_2 \sinh[K(L-z)], & a < z \leq L \\ c_2 \sinh[K(z-L)], & -L < z \leq -a \end{cases} \quad (\text{B5})$$

and the equations derived from the boundary conditions are

$$-\xi \cot \xi = \frac{m^*}{m} \eta \coth(\alpha\eta) \quad (\text{B6})$$

together with Eq. (B3b). In this case there is one solution for each value of ξ over the ranges $\Delta\xi_n + (n-1)\pi/2$ to $n\pi/2$ with $n=2,4,6,\dots$, where $\Delta\xi_n < \pi/2$ is a small, positive value that satisfies Eq. (B6) with $\eta \rightarrow 0$. An iterative solution for $\Delta\xi_n$ is found to be

$$\Delta\xi_n^{(i+1)} = \tan^{-1} \left(\frac{m^*}{m\alpha \left[(n-1)\frac{\pi}{2} + \Delta\xi_n^{(i+1)} \right]} \right) \quad (\text{B7})$$

with $\Delta\xi_n^{(0)} = \tan^{-1}(m^*/(m\alpha))$. To evaluate the solutions for ξ and η we now use

$$\xi^{(i+1)} = \tan^{-1} \left(\frac{m^*}{m\xi^{(i)}} \eta^{(i)} \coth(\alpha\eta^{(i)}) \right) + (n-1)\frac{\pi}{2} \quad (\text{B8})$$

again with $\xi^{(0)} = n\pi/2$. This scheme is applicable only for up to a maximum even n value such that $n\pi/2 \leq c\sqrt{m^*}$. If, for the next even n value, $c\sqrt{m^*}$ has a value such that $\Delta\xi_n + (n-1)\pi/2 \leq c\sqrt{m^*} < n\pi/2$, then a final solution exists with

$\Delta\xi_n + (n-1)\pi/2 \leq \xi \leq c\sqrt{m^*}$. Again, we employ a simple 1D numerical search to find that solution.

Before discussing the case of extended states of a conduction band we first deal with bound states of a valence band, again taking the band edge to be located at an energy V_0 below the vacuum level. We maintain our use of $\hbar^2 k_z^2 / (2m^*) = E_\perp$, but now the energies are measured downwards from the top of the valence band, so that $\hbar^2 K^2 / (2m) = \tilde{V}_0 + E_\perp$. In this case we have, instead of Eq. (B3b), the following relationship between ξ and η ,

$$-\frac{\xi^2}{m^*} + \eta^2 = c^2. \quad (\text{B9})$$

The same iterative schemes given in Eqs. (B6) and (B7) are still applicable, except that in both cases we now have $\eta^{(i)} \equiv \sqrt{c^2 + (\xi^{(i)})^2 / m^*}$. Solutions for ξ exist up to arbitrarily large values, so there are no special cases to consider for the final ξ values.

Returning to the case of extended states ($E > V_0$) of the conduction band, we have for even-parity states the perpendicular wavefunctions

$$\Phi_{k_z}(z) = \begin{cases} c_1 \cos(k_z z), & -a < z \leq a \\ c_2 \cos[K(L-z)], & a < z \leq L \\ c_2 \cos[K(z-L)], & -L < z \leq -a. \end{cases} \quad (\text{B10})$$

Application of the boundary conditions yield the implicit equations for ξ and η

$$\xi \tan \xi = -\frac{m^*}{m} \eta \tan(\alpha \eta) \quad \text{and} \quad (\text{B11a})$$

$$\frac{\xi^2}{m^*} - \eta^2 = c^2. \quad (\text{B11b})$$

Graphical and/or iterative solutions of these implicit equations are somewhat more complex than for the confined states, and numerous solutions for ξ (and η) can exist on any given $\pi/2$ interval of ξ . A general method for find these values is complicated by the fact that solutions of Eq. (B11a) alone for $\xi(n)$ can have slopes that can be very large or very small (depending on the value of η), thereby leading to instabilities in any simple iterative approach. Hence we employ a numerical search to find the solutions: incrementing ξ in suitably small steps (starting from $c\sqrt{m^*}$), computing $\eta = \sqrt{(\xi^2 / m^*) - c^2}$, and examining the expression $\xi \tan \xi + m^* \eta \tan(\alpha \eta) / m$ for a change in sign.

Finally, for odd-parity extended states the perpendicular wavefunctions are

$$\Phi_{k_z}(z) = \begin{cases} c_1 \sin(k_z z), & -a < z \leq a \\ c_2 \sin[K(L - z)], & a < z \leq L \\ c_2 \sin[K(z - L)], & -L < z \leq -a. \end{cases} \quad (\text{B12})$$

Application of the boundary conditions leads to

$$-\xi \cot \xi = \frac{m^*}{m} \eta \cot(\alpha \eta) \quad (\text{B13})$$

together with Eq. (B11b). These two equations are solved simultaneously in an analogous manner as for Eqs. (B11a) and (B11b).

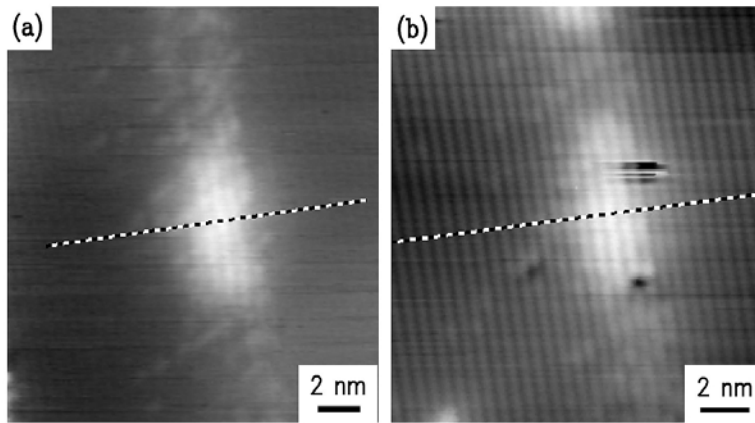


FIG 1. STM images of two QDs, showing location of topographic cuts through each QD. Growth direction is from right to left across each image. Both images were acquired with sample voltage of -2 V , and are displayed with gray scale ranges of (a) 0.26 and (b) 0.24 nm.

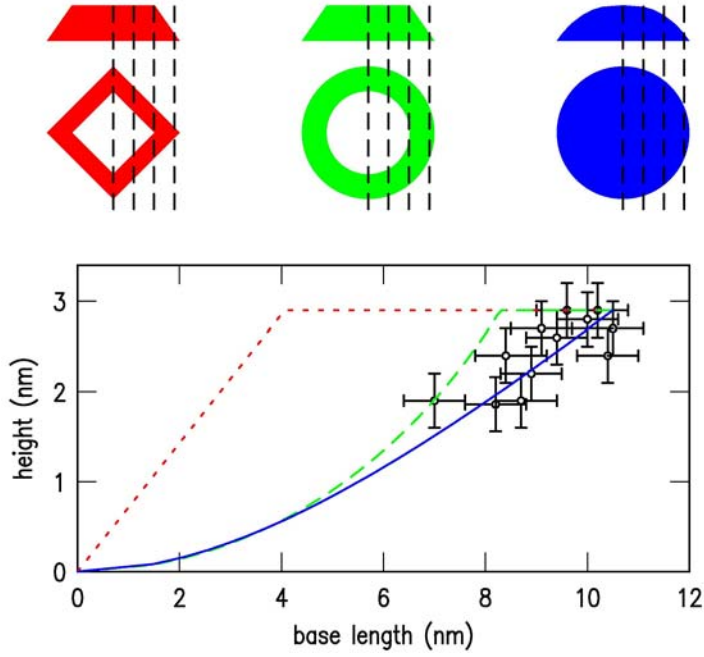


FIG 2. (Color online) Distribution of QD base lengths and heights, compared to theory for various shapes of the dots: truncated trapezoid – dotted line; truncated cone – dashed line; lens shape – solid line. The shapes are pictured in the upper part of the figure, together with a few possible locations of the cleavage plane.

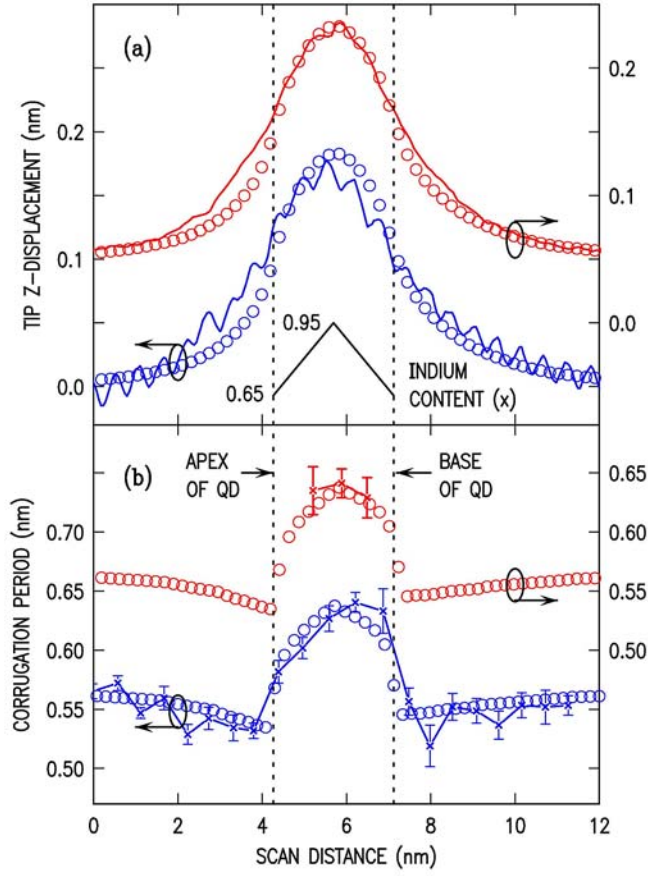


FIG 3. (Color online) (a) Cross-sectional topographic cuts and (b) corrugation period (local lattice parameter), measured along the dashed lines in Figs. 1(a) and (b) (upper and lower data sets, respectively). Experimental results are shown by solid lines, and results of finite-element computation by circles. The inset in (a) shows the step-graded composition profile for the QD used in the computations.

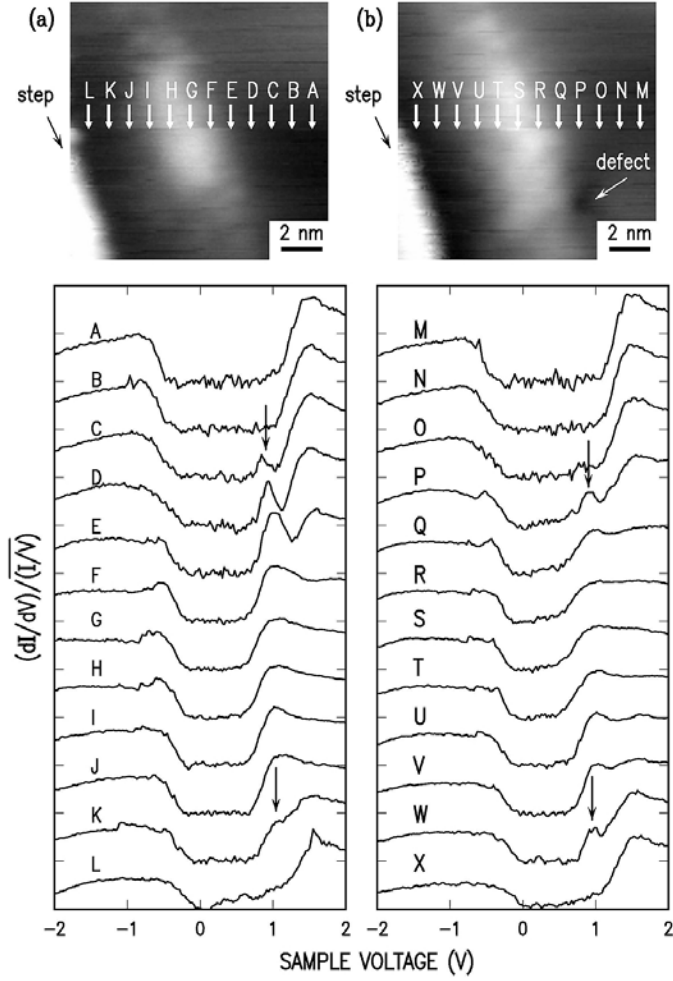


FIG 4. STM images (upper) and associated tunneling spectra (lower) from two InAs QDs, (a) and (b). Spectra are acquired at the locations marked in the images, and are displayed below each image. Neighboring locations for the spectra are separated by 1.0 nm. A spectral peak associated with each QD is marked by the arrows, for spectra acquired 3-4 nm from the center of the QDs. At locations closer to the QD this feature greatly broadens. An atomic step is located about 6 nm from the center of each QD, as indicated, and a point defect (vacancy) appears in (b), as shown. STM images were acquired at a sample voltage of -2 V, and are displayed with gray scale range of 0.2 nm.

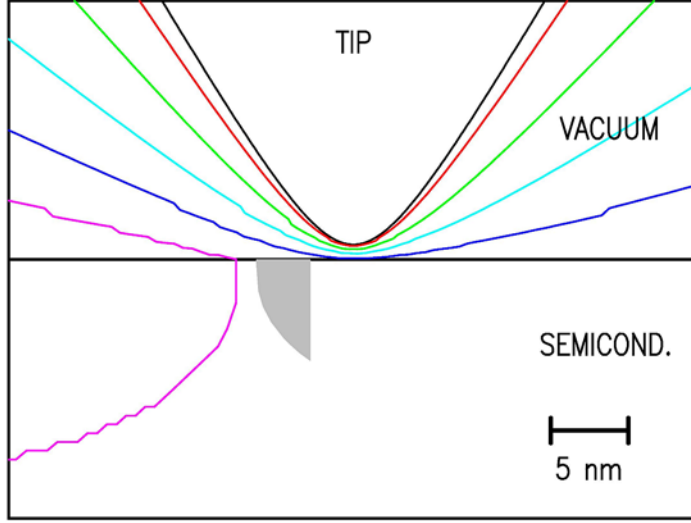


FIG 5. (Color online) Finite-element solution for the electrostatic potential in the semiconductor and vacuum, with a 2-nm radius-of-curvature probe-tip located 1.0 nm from the surface. The sample-tip voltage is set at +1.0 V and the contact potential between tip and sample is -0.87 eV, so the electrostatic potential energy of the tip relative to a point deep inside the semiconductor is +0.13 eV. Contours are shown for potential energies (eV) of 0.155 (red), 0.232 (green), 0.310 (cyan), 0.388 (blue), 0.465 (magenta). At distances further inside the semiconductor the potential falls gradually to 0 eV. The tip apex is positioned 4 nm from the center of a lens-shaped QD (shown in gray), and a strip of charge density associated with a surface step is located 6 nm on the other side of the QD (the physical step is not represented in the theory, only the charge density associated with the step). A constant state-density throughout the bandgap arising from the step is assumed, with value $2.5 \text{ nm}^{-1} \text{ eV}^{-1}$ and charge-neutrality level 0.25 eV above the VB maximum.

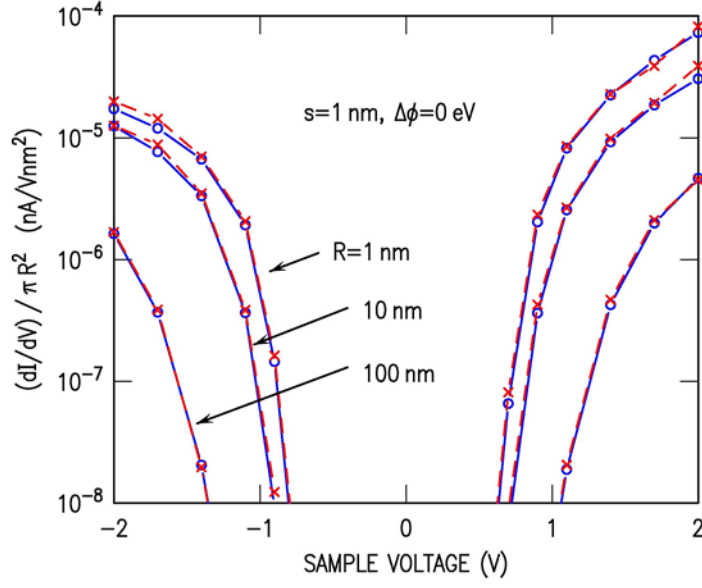


FIG 6. (Color online) Comparison of theoretical results for a tunneling spectrum using the plane-wave expansion method developed in the present work (red x-marks and dashed lines) to those obtained by numerical integration of the Schrödinger equation along the central axis of the problem as in Ref. [21] (blue circles and solid lines). Computations are for undoped GaAs with no surface states, using tip-sample separation of 1 nm, contact potential of 0 eV, and tip radii of 1, 10, and 100 nm as shown.

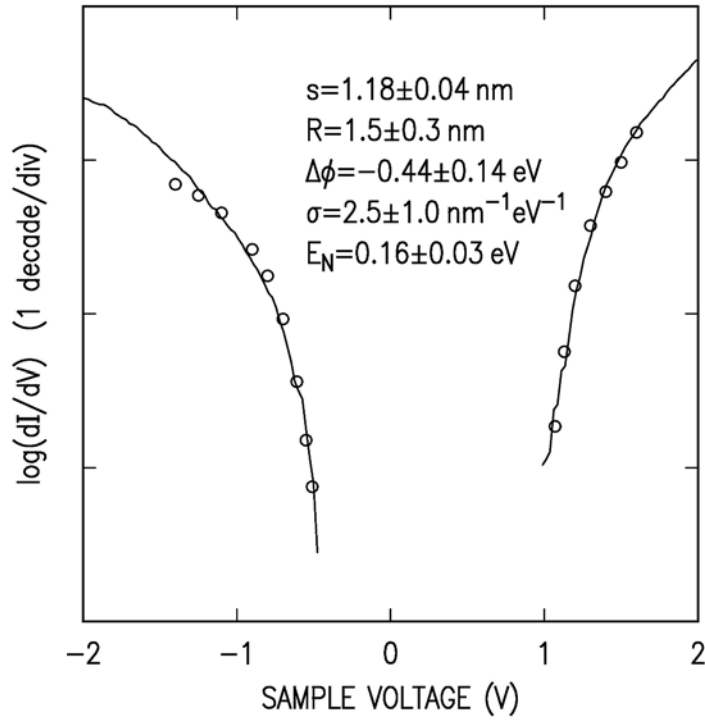


FIG 7. Spectrum of GaAs(110) surface from spectrum A of Fig. 4(a), acquired 6 nm from the quantum dot. Experiment is shown by the lines and theory by the circles. Values of the parameters from the fit are listed (see text).

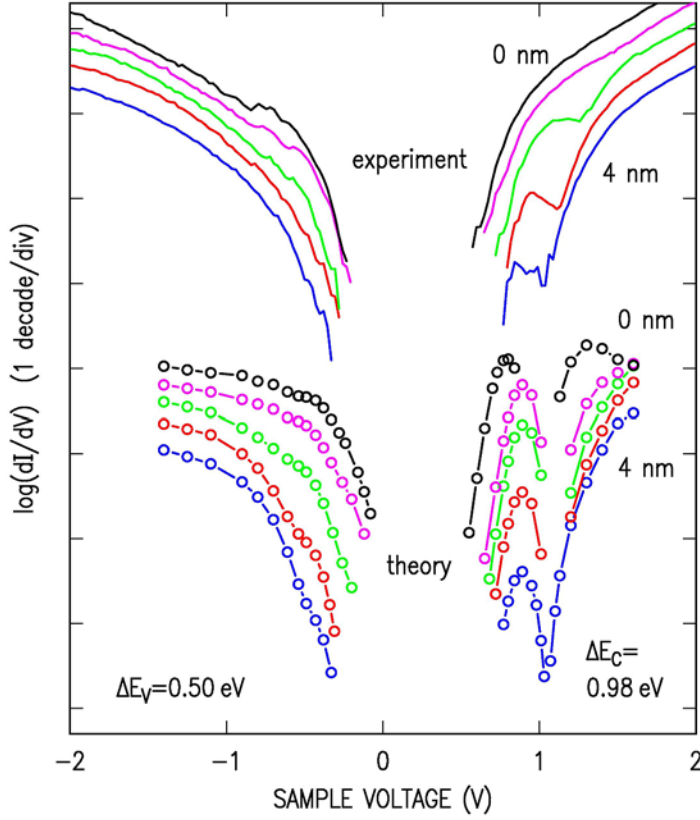


FIG 8. (Color online) Upper: Experimental conductance spectra, acquired at 0, 1, 2, 3, and 4 nm from the QD, corresponding to spectra G, F, E, D, and C, respectively, of Fig. 4. Lower: Theoretical results, computed using the same parameter values as in Fig. 7 along with values for the band offsets ΔE_V and ΔE_C as listed. Spectra are shifted from each other along the vertical axis for ease of viewing. A negative differential-conductance region around +1.1 V occurs for the theoretical curves at 0, 1, 2, and 3 nm from the QD, and is not shown in the plot.

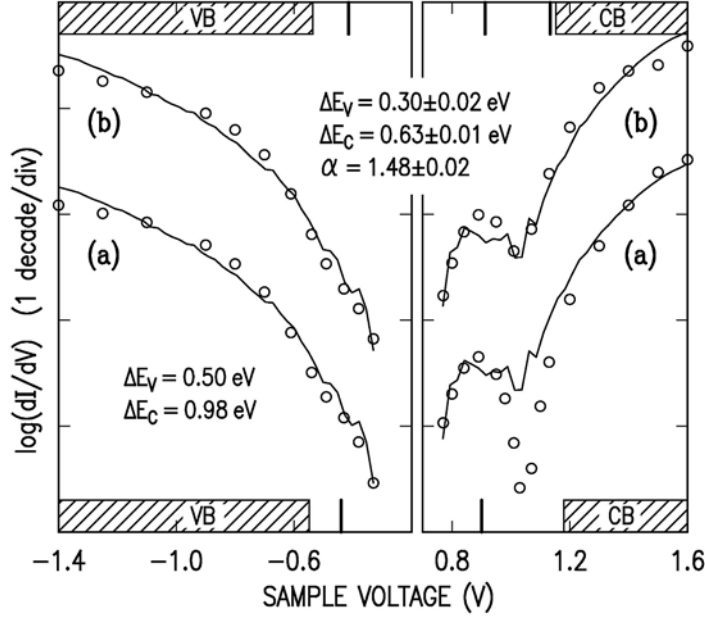


FIG 9. Comparison of experiment and theory for the spectrum acquired 4 nm from the QD. Experimental results are shown by the solid lines, repeated twice. Theoretical results are shown by circles for the same parameter values as in Fig. 7, together with (a) parameter values for the band offsets ΔE_V and ΔE_C , or (b) values for ΔE_V and ΔE_C along with an additional parameter α that expands the QD size thereby producing a greater number of QD states. In the upper and lower parts of the figure are shown the energy levels from the fits, plotted in terms of the voltages for which the Fermi-level of the tip is aligned with each energy level. Vertical lines indicate the QD confined states (for the VB, only light-hole states are shown), and the hatched regions show unconfined VB and CB states in the near surface region. For fit (a), only a single confined electron state occurs, but for fit (b) two states are found (the second state lying very close to the CB edge).

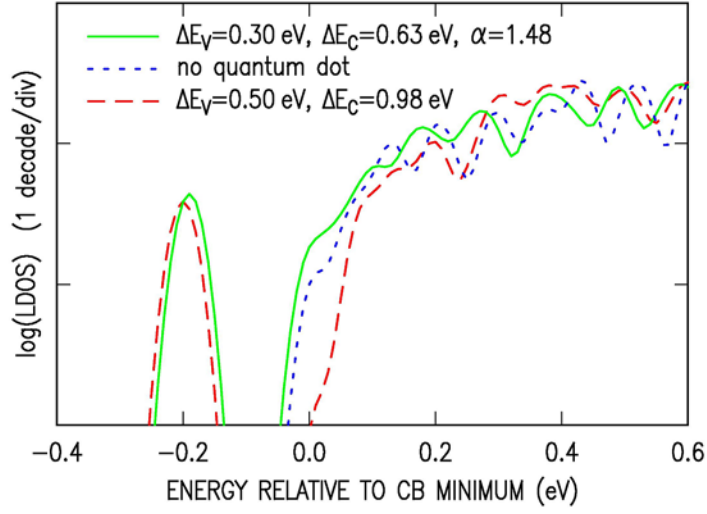


FIG 10. (Color online) Theoretical LDOS, on a logarithmic scale, for the two models used to fit the data in Fig. 9 (dashed red line and solid green line), together with the LDOS for the system without any quantum dot (dotted blue line). A Gaussian broadening of 0.055 eV FWHM has been used in computing the LDOS. The electron bound states is seen near -0.2 eV , and a resonance/anti-resonance occurs near 0 eV.

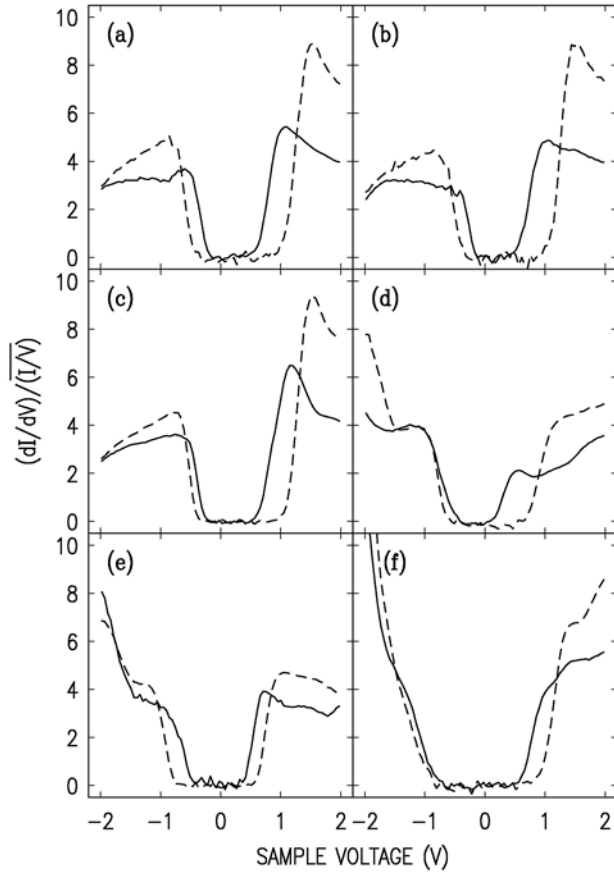


FIG 11. Summary of conductance spectra measured on (solid line) and off (dashed line) various QDs.

References

- ¹ D. Bimberg, M. Grundmann, and N.N. Lendentsov, *Quantum Dot Heterostructures* (Wiley, New York, 1998).
- ² B. Lita, R. S. Goldman, J. D. Phillips, and P. K. Bhattacharya, Appl. Phys. Lett. **74**, 2824 (1999).
- ³ H. Eisele, O. Flebbe, T. Kalka, C. Preinesberger, F. Heinrichsdorff, A. Krost, D. Bimberg, and M. Dähne-Preitsch, Appl. Phys. Lett. **75**, 106 (1999).
- ⁴ D. M. Bruls, J. W. A. M. Vugs, P. M. Koenraad, H. W. M. Salemink, J. H. Wolter, M. Hopkinson, M. S. Skolnick, Fei Long, and S. P. A. Gill, Appl. Phys. Lett. **81**, 1708 (2002).
- ⁵ J. H. Blokland, M. Bozkurt, J. M. Ulloa, D. Reuter, A. D. Wieck, P. N. M. Koenraad, P. C. M. Christianen, and J. C. Maan, Appl. Phys. Lett. **94**, 023107 (2009).
- ⁶ H. Eisele, A. Lenz, R. Heitz, R. Timm, M. Dähne, Y. Temko, T. Suzuki, and K. Jacobi, J. Appl. Phys. **104**, 124301 (2008).
- ⁷ T. Yamauchi, Y. Matsuba, L. Bolotov, M. Tabuchi, and A. Nakamura, Appl. Phys. Lett. **77**, 4368 (2000).
- ⁸ B. Legrand, B. Grandidier, J.P. Nys, D. Stiévenard, J.M. Gérard, and V. Thierry-Mieg, Appl. Phys. Lett. **73**, 96 (1998).
- ⁹ T. Maltezopoulos, A. Bolz, C. Meyer, C. Heyn, W. Hansen, M. Morgenstern, R. Wiesendanger, Phys. Rev. Lett. **91**, 196804 (2003).
- ¹⁰ J.-Q. Lu, H. T. Johnson, V. D. Dasika, and R. S. Goldman, Appl. Phys. Lett. **88**, 053109 (2006).
- ¹¹ A. Urbieto, B. Grandidier, J. P. Nys, D. Deremes, D. Stiévenard, A. Lemaître, G. Patriarche, and U. M. Niquet, Phys. Rev. B **77**, 155313 (2008).
- ¹² V. D. Dasika, R. S. Goldman, J. D. Song, W. J. Choi, N. K. Cho, and J. I. Lee, J. Appl. Phys. **106**, 014315 (2009).
- ¹³ J. C. Girard, A. Lemaître, A. Miard, C. David, and Z. Z. Wang, J. Vac. Sci. Technol. B **27**, 891 (2009).
- ¹⁴ L. W. Wang, J. Kim, and A. Zunger, Phys. Rev. B **59**, 5678 (1999).
- ¹⁵ O. Stier, M. Grundmann, and D. Bimberg, Phys. Rev. B **59**, 5688 (1999).
- ¹⁶ L. W. Wang, A. J. Williamson, A. Zunger, H. Jiang, and J. Singh, Appl. Phys. Lett. **76**, 339 (2000).
- ¹⁷ A. J. Williamson, L. W. Wang, and A. Zunger, Phys. Rev. B **62**, 12963 (2000).
- ¹⁸ V. Milnar, M. Bozkurt, J. M. Ulloa, M. Ediger, G. Bester, A. Badolato, P. M. Koenraad, R. J. Warburton, and A. Zunger, Phys. Rev. B **80**, 165425 (2009).
- ¹⁹ For a review, see R. M. Feenstra, Semicond. Sci. Technol. **9**, 2157 (1994).
- ²⁰ S. Gaan, G. He, R. M. Feenstra, J. Walker, and E. Towe, Appl. Phys. Lett. **97**, 123110 (2010).
- ²¹ Y. Dong, R. M. Feenstra, M. P. Semtsiv, and W. T. Masselink, J. Appl. Phys. **103**, 073704 (2008).
- ²² D. Pal and E. Towe, Appl. Phys. Lett. **88**, 153109 (2006).
- ²³ L. Chen, D. Pal, and E. Towe, J. Cryst. Growth **251**, 208 (2003).
- ²⁴ R. M. Feenstra, Physics B **273-274**, 796 (1999).
- ²⁵ We use the commercial package COMSOL, with elastic constants (in GPa) of $C_{11}=119$, $C_{12}=53.8$, and $C_{44}=59.9$ for GaAs, and $C_{11}=83.29$, $C_{12}=45.26$, and $C_{44}=39.59$ for InAs,

-
- all from *Semiconductors: group IV elements and III-V compounds*, ed. O. Madelung, (Springer-Verlag, Berlin, 1991).
- ²⁶ V. Ramachandran and R. M. Feenstra, Phys. Rev. Lett. **82**, 1000 (1999).
- ²⁷ M. Berthe, R. Stiufiuc, B. Grandidier, D. Deresmes, C. Delerue, and D. Stiévenard, Science **319**, 436 (2008).
- ²⁸ R. M. Feenstra, J. Vac. Sci. Technol. B **21**, 2080 (2003).
- ²⁹ R. M. Feenstra, Y. Dong, M. P. Semtsiv, and W. T. Masselink, Nanotechnology **18**, 044015 (2007).
- ³⁰ If accumulation or inversion of the confined state in the dot occurred then that would, of course, affect the electrostatics, but those situations do not occur in the present computations.
- ³¹ J. Tersoff and D. R. Hamann, Phys. Rev. B **31**, 805 (1985).
- ³² See, e.g., A. R. Smith, R. Yang, H. Yang, W. R. L. Lambrecht, A. Dick, J. Neugebauer, Surf. Sci. **561**, 154 (2004).
- ³³ I. Vurgaftman, J. R. Meyer, L. R. Ram-Mohan, J. Appl. Phys. **89**, 5815 (2001).
- ³⁴ The normalized conductance $(dI/dV)/(I/V)$ provides a very convenient means of viewing the data, but its use in quantitative analysis can lead to significant errors. Even for the case of evaluation of bulk band edge positions, significant errors can result if the spectra are not measured up to voltages sufficiently beyond the band edge (see Ref. [21]). For the present case of the QD confined states, we find that the positions of the onsets of the QD states are shifted significantly by the normalization procedure.
- ³⁵ In our fits, the computed spectra are found to be completely insensitive to the *number* of steps (1, 2, or more) placed on the QD layers other than the one near the tip, so the computations are done for a single step at of those layers. The steps themselves are spread out over some width, comparable to or greater than the grid spacing in the problem. For the step nearest the tip a width of 2 nm is used, for the nearest-neighbor steps a width of 10 nm is used, and all other steps are spread out over 50 nm thereby forming a spatially continuous sheet of surface states.
- ³⁶ As indicated in Fig. 7, a lower limit on the value of σ derived from the fitting is $1.5 \text{ nm}^{-1} \text{ eV}^{-1}$. Concerning an upper limit, the dependence of the sum-of-squared residuals (SSR) on σ is very non-parabolic, and we can actually obtain good fits for arbitrarily large values of σ . The reason for this lack of dependence of the SSR on the value of σ is that for large σ the Fermi-level is strongly pinned (in the vicinity of the steps).
- ³⁷ The onsets of the continua representing the VB or CB are located by finding where the next higher electron state (or lower hole state) that is *not* a bound state is aligned with the tip Fermi level. This procedure is appropriate for the present case of a small number of k-values and a correspondingly small unit cell size for the computation (see Section III); the band edges represented in these distributions should thus be interpreted as the band edges in the *near-surface* region. To find the actual number of bound states for each band, a computation is performed *without* the presence of any band bending, so that the bound states can be easily identified since their energies are beyond the band edges.
- ³⁸ M. Nagashima, M. Kibe, M. Doshida, Y. Uchiyama, Y. Matsukura, and H. Nishino, J. Appl. Phys. **107**, 054504 (2010).
- ³⁹ J. Bardeen, Phys. Rev. Lett. **6**, 57 (1961).

-
- ⁴⁰ C. B. Duke, *Tunneling in Solids* (Academic Press, New York, 1969), p. 217.
- ⁴¹ J. Tersoff, Phys. Rev. B **41**, 1235 (1990).
- ⁴² E. Merzbacher, *Quantum Mechanics*, 2nd ed. (Wiley, New York, 1970), p. 105-108.